$LaAu_2$ and $CeAu_2$ surface intermetallic compounds grown by high-temperature deposition on Au(111)

M. Ormaza,[1] L. Fernández,[2] S. Lafuente,[1] M. Corso,[3] F. Schiller,[4] B. Xu,[5] M. Diakhate,[5] M. J. Verstraete,[5] and J. E. Ortega[1,2,4]

[1]*Universidad del País Vasco UPV-EHU, Departamento Física Aplicada I, E-20018 San Sebastián, Spain*

[2]*Donostia International Physics Center, Paseo Manuel Lardizabal 4, E-20018 San Sebastián, Spain*

[3]*IKERBASQUE, Basque Foundation for Science, 48011 Bilbao, Spain*

[4]*Centro de Física de Materiales CSIC/UPV-EHU-Materials Physics Center, Manuel Lardizabal 5, E-20018 San Sebastián, Spain*

[5]*Université de Liège, Institut de Physique, Allée du 6 Août, 17 Sart-Tilman B-4000 Liège, Belgium*

(Received 11 June 2013; revised manuscript received 14 August 2013; published 3 September 2013)

We report on the crystal structure and electronic bands of $LaAu_2$ and $CeAu_2$ surface intermetallic compounds grown by high-temperature deposition on Au(111). By scanning-tunneling microscopy we study the formation of different alloy phases as a function of growth temperature and lanthanide coverage. We determine the specific growth conditions to achieve monolayers and bilayers of $LaAu_2$ and $CeAu_2$ with high crystalline quality. Due to lattice mismatch with the underlying Au substrate, both $LaAu_2$ and $CeAu_2$ exhibit long-range moiré patterns, which can serve as templates for further nanostructure growth. By angle-resolved photoemission we map the two-dimensional band structure of these surface alloys, discussing the nature of the different spectral features in the light of first-principles calculations.

DOI: 10.1103/PhysRevB.88.125405 PACS number(s): 73.61.At, 73.22.−f

I. INTRODUCTION

The ability to control and modify the structure and electronic properties of surfaces is of key importance in developing technologically relevant materials. Surface alloying is a straightforward route to tuning surface electronic states and geometric structure. From the electronic point of view, the tunable chemical composition of the surface layer is of great importance, e.g., to optimizing catalytic processes,[1,2] and in general to tailoring exotic nanoscale electronic properties. Structurally, surface-confined alloying can be exploited, e.g., to tune moiré patterns and dislocation networks, which characterize many metal overlayer systems with lattice mismatch. Such periodically modulated surfaces have great potential as nanotemplates for self-organized growth of nanostructures.[3–6]

The $GdAu_2$ intermetallic compound is a good example of a periodically modulated metallic surface induced by alloying.[3,7,8] High-temperature deposition of Gd on Au(111) gives rise to stable $GdAu_2$ mono and bilayers with a high crystalline quality that present long-range moiré patterns. This system has been shown to behave as a very effective nanoscale template for highly dense Co nanodot arrays.[3] The full structural and electronic characterization of both monolayers and bilayers demonstrates that such a $GdAu_2$ surface alloy is actually a novel phase, with distinct layer stacking compared to the bulk $GdAu_2$ crystal.[7] Additionally, exotic magnetic properties are predicted, which may have strong influence on the magnetic anisotropy of Co nanodots that nucleate in the moiré lattice.[9]

In this work we apply the same high-temperature growth procedure to lanthanum and cerium, on Au(111). These two elements are particularly attractive to investigate the role of the substrate in the magnetic properties of nanodot arrays. Compared to Gd, La and Ce have similar valence electronic states but different numbers of $4f$ electrons, i.e., those that determine the special magnetism of rare-earth (RE) metals.[10,11] La does not have $4f$ e^- and hence is not magnetic, whereas Ce metal possesses two $4f$ e^- and is known to behave magnetically in a very peculiar way.[12–15] We demonstrate that both La and Ce form surface-confined intermetallic compounds on Au(111), in a similar way to $GdAu_2$.[8] In light of angle-resolved photoemission spectroscopy (ARPES), scanning-tunneling microscopy (STM) experiments, and first-principles theory we discuss the nature, analogies, and differences in electronic states and structure among these three surface alloys.

II. EXPERIMENT AND THEORY DETAILS

Scanning-tunneling microscopy experiments were performed in an Omicron variable-temperature STM setup operating at 300 K. ARPES experiments were carried out at the plane grating monochromator (PGM) beamline of the Synchrotron Radiation Center (SRC) in Stoughton, Wisconsin. We used a hemispherical Scienta SES200 spectrometer with energy and angular resolution set to 25 meV and 0.2°, respectively and p-polarized light. La and Ce were deposited from electron-beam evaporators at a base pressure below $p = 5 \times 10^{-9}$ mbar, and with the Au(111) single-crystal sample held at different temperatures. The substrate temperature during the evaporation of La and Ce is crucial to optimizing the homogeneity and extension of the moiré structure. Substrate temperatures used for evaporation varied around 780 K for La and between 650 and 750 K for Ce. Below these temperatures the moiré is not well formed or other phases dominate, and above them, the RE metal fades away into the bulk or re-evaporates to vacuum. The optimal substrate temperature in each case was fixed in the ARPES measurements, where we could track the evolution of the electronic structure as a function of the thickness by evaporating RE-metal films as linear wedges. These could be accurately scanned thanks to the small size of the synchrotron beam (100 μm). The lanthanide coverage in STM experiments is expressed in evaporation minutes, whereas in ARPES experiments we refer to alloy

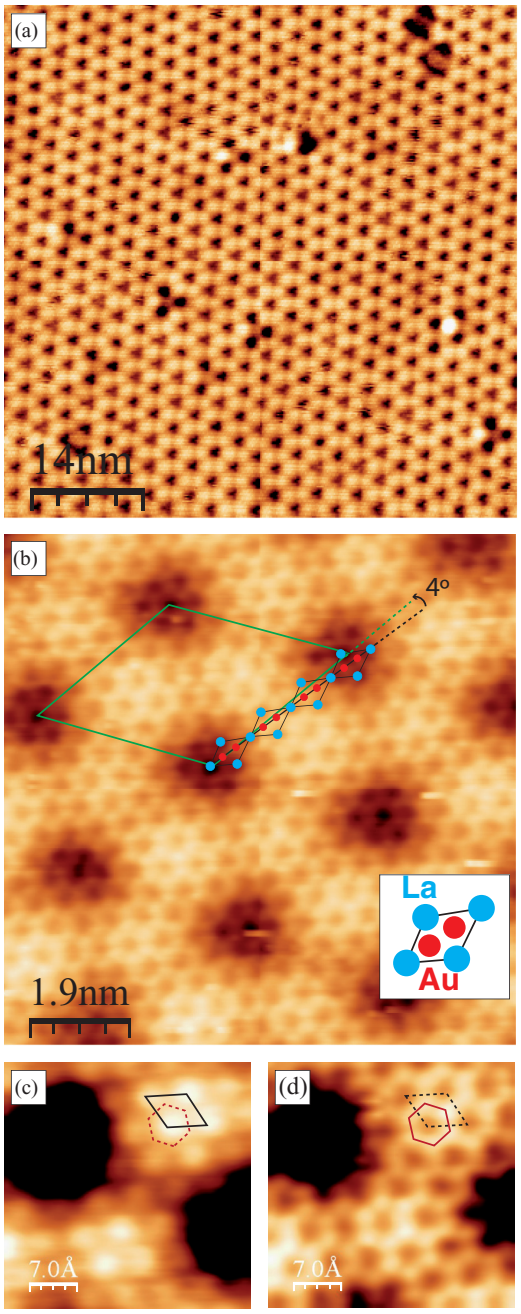

FIG. 1. (Color online) STM images of the $LaAu_2$ surface intermetallic compound taken at different length scales. (a) At a large scale, the hexagonal moiré superstructure is characterized by slightly undulated rows of triangles. (b) The wavy appearance of the moiré is linked to a variable misalignment of the atomic lattice with respect to the moiré structure, with a maximum of 4°, as shown in the overlaid drawing. The $LaAu_2$ unit cell is sketched in the inset. (c) and (d) Atomically resolved STM images of the $LaAu_2$ surface alloy revealing one protrusion (La) per unit cell (marked black) in (c) and two protrusions (Au atoms) in a honeycomb arrangement (marked red) in (d). Image parameters: (a, b) −2 V, 0.1 nA, (c) −2 V, 1 nA, and (d) −2 V, 0.1 nA.

monolayers (ML), as determined from the sharpness of the band features on the evaporated wedges.

Calculations for the surface intermetallic compounds are carried out within the framework of density functional theory, using the ABINIT package.[16] We adopt the local density approximation and the projector augmented-wave method,[17] with a plane-wave cutoff energy of 20 hartree (Ha). The potentials of La, Ce, and Au are constructed with 11, 12, and 11 valence electrons, and with cutoff radii of 3.02, 2.51, and 2.69 bohr, respectively. For each angular momentum channel, two projectors are used. A $\sqrt{3} \times \sqrt{3}$ unit cell ($d_{\sqrt{3}\times\sqrt{3}} = 4.99$ Å) is used for the alloy, with seven layers of Au substrate and a minimum of 8.3 Å of vacuum between periodic slab images. Good convergence for the bulk Au states is achieved with the k-point sampling in the Brillouin zone on an unshifted 12×12 grid. To include the strong correlation of f electrons, the LDA + U method is used. The Hubbard parameters are $U = 8.0$ eV and $J = 0.7$ eV for La, and $U = 6.1$ eV and $J = 0.7$ eV for Ce.[18] The Ce calculations are performed with collinear spin polarization, which allows the description of the magnetic states.

Three different surface structures have been considered for the alloy layers, one on-top (primitive hexagonal stacking ···ABCABCA**A**) and two hollow configurations (fcc ···ABCABCA**B** and hexagonal close packed ···ABCABCA**C**), relative to the atomic positions of the Au sublayer below the monolayer (ML). After fixing the in-plane lattice constant to the theoretically relaxed Au bulk value, the structures were optimized, allowing the ML and two Au sublayers to relax, until the forces on atoms were less than 1×10^{-5} Ha/bohr. The ground state is given by the fcc hollow configuration. In the La case the hcp hollow surface structure is slightly unfavorable, but the hexagonal on-top configuration is significantly higher than the ground state (583 meV/unit cell for $LaAu_2$). For $CeAu_2$, consistent with $LaAu_2$, the ground state is the fcc hollow structure, which is lower in energy than the on-top configuration by 289 meV/unit cell. These energies are not dependent on the chemical potential. The moiré structure will yield different alloy alignments in different regions of the substrate, but we proceed using the most stable hollow structure as a reference. All three configurations yield ferromagnetic states for Ce, with magnetizations of about 1 μ_B that arise from the $4f$ electrons.

III. RESULTS

A. Growth of $LaAu_2$ and $CeAu_2$ surface intermetallic compounds

Figures 1–3 show characteristic STM images taken after the high-temperature deposition of La (Fig. 1) and Ce (Figs. 2 and 3) on Au(111) at different length scales. We observe a complete analogy with the case of $GdAu_2$.[8] It is possible to tune the deposition parameters to obtain the pure $LaAu_2$ surface phase with its characteristic moiré pattern. In fact, homogeneous $LaAu_2$ moiré patterns with the highest crystal quality, and extending over the whole surface are achieved with the substrate held at 780 K. The lattice periodicity of the moiré is (32 ± 2) Å, as determined from the large-scale view in Fig. 1(a). The nearest neighbor distance (5.3 ± 0.3) Å measured in the atomically resolved image in Fig. 1(b) corresponds to the size of the unit cell of the $LaAu_2$ overlayer, which is depicted in the inset of Fig. 1(b). Figures 1(c) and 1(d) reveal a variable atomic contrast within the unit cell,

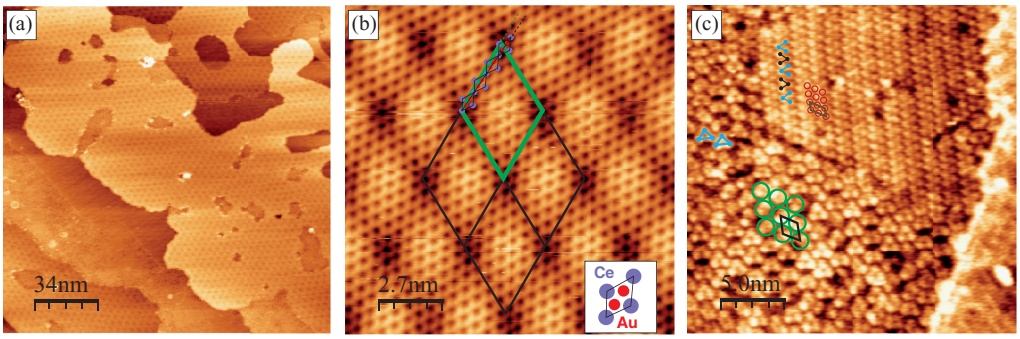

FIG. 2. (Color online) (a) Large-scale STM view obtained after evaporation of Ce on Au(111) at 750 K. Around 70% of the surface is covered by CeAu$_2$ moiré phase. (b) Atomically resolved STM images of the CeAu$_2$ moiré phase. The inset shows the CeAu$_2$ unit cell. In the image, the large unit cell marks the moiré superstructure while the small hexagonal unit cell refers to the CeAu$_2$ atomic lattice. (c) Morphology of the Ce-Au alloy at triangular cluster areas away from the CeAu$_2$ moiré lattice. The three lobes that form a single cluster are arranged forming a triangle. The circles in the bottom part of the image denote the quasihexagonal arrangement, where each circle represents a cluster. The surface unit cell is marked in black. The triangular clusters with a double-chain structure display an overall rectangular surface unit cell that is represented by the small circles in the top part of the image. Image parameters: (a) −1.5 V, 0.5 nA, (b) 0.05 V, 2 nA, and (c) 1 V, 1 nA.

which exclusively depends on the tunneling current I_t, i.e., the tip sample distance. At bias voltages ($U_b = -2$ V), far from the Fermi level (E_F), and $I_t = 1$ nA the unit cell is featured as a single protrusion, while for $I_t = 0.1$ nA we clearly define a honeycomb arrangement. A straightforward interpretation assigns the protrusions to La atoms in the former image, and to the pair of Au atoms in the latter one.

As in GdAu$_2$, the moiré arises due to the superposition of the different LaAu$_2$ and Au(111) lattices. Both STM and low-energy electron diffraction (LEED) measurements reveal that the LaAu$_2$ atomic lattice is rotated by 30° with respect to the Au(111) substrate. The La-Au in-plane distance $d_{\text{La-Au}} = (3.1 \pm 0.2)$ Å deduced from Figs. 1(b)–1(d) is larger than the Au(111) substrate lattice constant (nominally, 2.88 Å), giving rise to a coincidence of the hexagonal (10.4 × 10.4) LaAu$_2$ lattice with the (11.4 × 11.4) Au(111) lattice, which explains the moiré. The LaAu$_2$ overlayer is thus incommensurate with respect to the Au(111) substrate, which is reflected by local deviations in the moiré periodicity. Random atom vacancies and defects, visible in Fig. 1(a), are more frequent than in GdAu$_2$ and may be partly triggered by such lattice incommensurability. On the other hand, the hexagonal moiré lattice in Fig. 1(b) appears rotated by ∼30° with respect to the LaAu$_2$ atomic lattice, in agreement with LEED measurements. In reality, the azimuthal misalignment of the moiré and the atomic lattices varies smoothly within −4° to 4° across the surface. This variation explains the wavy aspect of the superlattice in large-scale images, such as that of Fig. 1(a), and reflects again the incommensurability of the LaAu$_2$ and Au(111) atomic lattices.

The high-temperature growth of a pure CeAu$_2$ compound with optimum morphology and crystallinity is more difficult than in the case of LaAu$_2$ or GdAu$_2$. The evaporation of Ce on Au(111) at temperatures between 650 and 750 K gives rise to the formation of different reacted phases that coexist with the CeAu$_2$ moiré. The best results have been obtained by holding the substrate temperature at 750 K. In this case, a 1 ML thick CeAu$_2$ moiré phase homogeneously extends to about 70% of the surface, coexisting with (CeAu)-triangular clusters distributed in small areas. The characteristic morphology at a large scale is shown in Fig. 2(a), whereas Fig. 2(b) shows the atomically resolved STM image of the CeAu$_2$ moiré phase. The latter exhibits a superperiodic unit cell with (33 ± 2) Å lattice constant, and a nearest neighbor distance of (5.4 ± 0.3) Å, which corresponds to the CeAu$_2$ surface unit cell dimensions. As in Fig. 1(d) for LaAu$_2$, at these particular tunneling conditions the unit cell protrusions define the honeycomb-like structure expected for the Au atom sublattice. Similar to that for Gd and La, the moiré pattern reflects the mismatch between the in-plane Ce-Au atomic distance [$d_{\text{Ce-Au}} = (3.1 \pm 0.2)$ Å] in the alloy and the atomic distance in the Au(111) surface. In the same way as Gd and La, the CeAu$_2$ is 30° rotated with respect to the Au(111) plane. This results in a coincidence lattice of (10.6 × 10.6) CeAu$_2$ on top of a (11.6 × 11.6) Au(111), suggesting that the CeAu$_2$ overlayer is incommensurate with the Au(111) substrate, as in the case of La. The moiré pattern also exhibits an average 30° rotation with respect to the surface unit cell of CeAu$_2$, with a smoothly varying misalignment analogous to that of LaAu$_2$, as indicated in Fig. 2(b).

Figure 2(c) examines the (Ce-Au)-triangular clusters that coexist with the CeAu$_2$ moiré structure. The clusters are apparently formed by three spherical lobes arranged in a triangle-like geometry and can be found forming hexagons (bottom part of the image) or double chains (top part of the image). Those arranged as double chains present an ordered phase with a rectangular surface unit cell of 17.2 × 14.5 Å, while the hexagonal clusters lack long-range order. We can refer in this case to a quasihexagonal arrangement with a nearest neighbor distance around 14.5 Å. There are similarities between both structures, and it seems that the quasihexagonal phase is a precursor of the double chain. In the latter case the three lobes are ordered forming well-defined, close-packed triangles that give place to chains, as marked in Fig. 2(c).

The triangular cluster phase can only be eliminated by lowering the substrate temperature to 650 K. In such a case, the CeAu$_2$ phase is the only one observed, but the surface becomes rougher, i.e., three-dimensional CeAu$_2$ islands develop on top of a CeAu$_2$ interface layer (Fig. 3). The CeAu$_2$ islands exhibit both monolayer and bilayer heights, i.e., 2.2 and 4.5 Å,

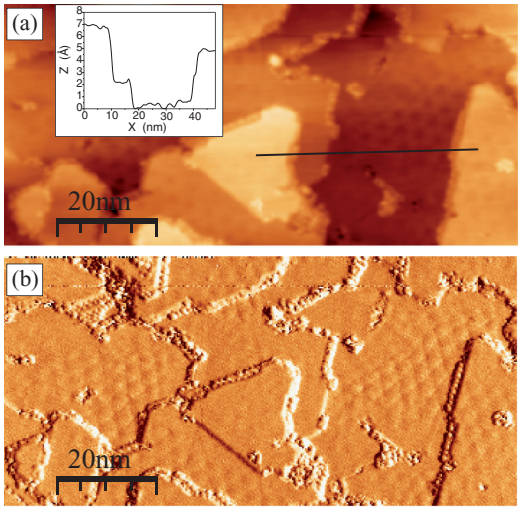

FIG. 3. (Color online) STM pictures for Ce evaporated on Au(111) at 650 K. The growth conditions permit the nucleation of a pure $CeAu_2$ moiré phase, eliminating the triangular clusters of Fig. 2(c). However, the lower substrate temperature leads to a rougher morphology with coexisting monolayer and bilayer islands. (a) Topography and line profile. (b) Current image enhancing the moiré corrugation, which is attenuated in 2 ML thick islands with respect to the 1 ML structure.

respectively. These values equal the interlayer distance of 2.2 Å for $GdAu_2$, as determined by x-ray photoelectron diffraction.[7] The tunneling current image in Fig. 3(b) shows the evolution of the moiré pattern with the number of layers. The moiré pattern on top of the islands becomes weaker and eventually disappears as the interface stress is released [see Fig. 3(b)]. On the other hand, a further reduction of the evaporation temperature down to 300 K leads to another family of alloys with reduced Au content,[19] as also observed in the case of Gd.[8] In this case, the $CeAu_2$ stoichiometry and its characteristic moiré can be recovered after post-annealing to 750 K, but its relative proportion with respect to other Ce-Au reacted phases is much lower than the 70% maximum obtained by direct growth at 750 K.

B. Electronic states

The two-dimensional (2D) electronic band structure of $LaAu_2$ and $CeAu_2$ surface compounds are obtained by angle-resolved photoemission. These experiments were performed on wedge-evaporated samples, which allows one to accurately define 1 and 2 ML coverages. The 1 ML point in the wedge is determined by the complete quenching of the Shockley surface state of the Au(111) substrate, whereas the thickness beyond 1 ML is controlled with the Au $4f$ core-level intensity. However, due to the inherent difficulties of mimicking the STM growth conditions (temperature, flux) to obtain the purest $LaAu_2$ and $CeAu_2$ phases, a general consistency is sought with all, surface state and core-level intensity analysis, quartz microbalance reading, and valence band spectral features (discussed below), and comparing with the already studied $GdAu_2$ alloy.[8] For the sake of comparison, $GdAu_2$ data are included in valence-band spectra in Figs. 6 and 7.

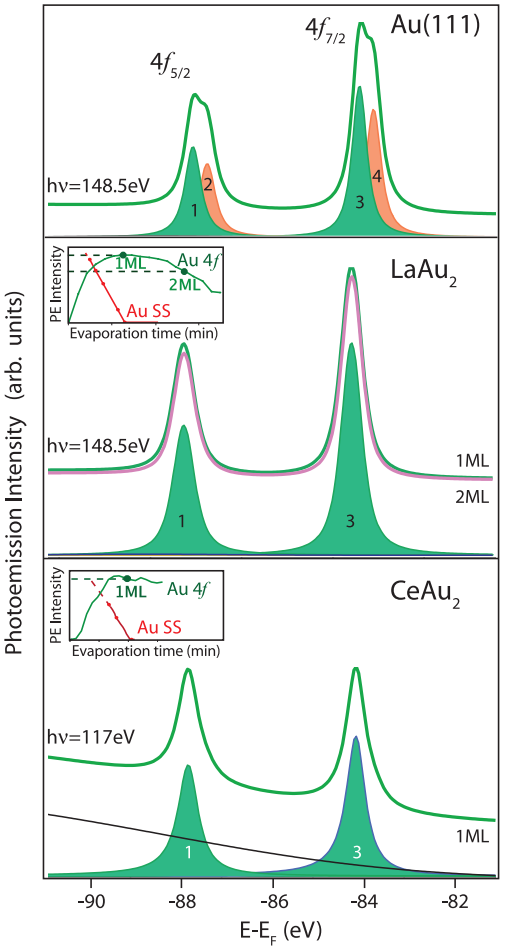

FIG. 4. (Color online) $4f$ Au core-level spectra for Au(111) compared to one and two monolayers of $LaAu_2$ and one monolayer of $CeAu_2$, both grown by high-temperature deposition. Surface core-level shifts are marked as peaks 2 and 4. The $4f$ component related to the surface alloy appears slightly shifted with respect to bulk Au metal (peaks 1 and 3). The insets show the intensity (peak height) variation of the Shockley surface state of Au(111) and the Au $4f$ intermetallic compound core-level line (peak 3) across the evaporated wedges of La and Ce. The surface state quenching marks the 1 ML coverage.

Figure 4 illustrates the transformation of Au $4f$ core levels after $LaAu_2$ and $CeAu_2$ growth, presenting a completely analogous behavior compared to the synthesis of the $GdAu_2$ surface alloy.[7,8] The spectrum spans the entire Au $4f$ core-level region, including the two spin-split components $4f^{5/2}$ and $4f^{7/2}$. Peaks labeled 2 and 4 correspond to the surface core-level shift of Au, whereas peaks 1 and 3 correspond to Au atoms in both the alloy and the bulk crystal. These cannot be resolved, although a smooth shift of $\Delta E = 70$ meV (60 meV in Ce) to higher binding energies is observed from the pure bulk component to the alloy. As shown in the corresponding insets, the intensity of the Au surface state goes to zero across the wedge at the same rate at which the alloy/bulk peak intensity increases and reaches its maximum. For La, the core-level intensity decreases for 2 ML, as expected from the attenuation effect of La atoms in thicker alloy films. For Ce, the bulk/alloy Au $4f$ signal remains constant beyond 1 ML, indicating that

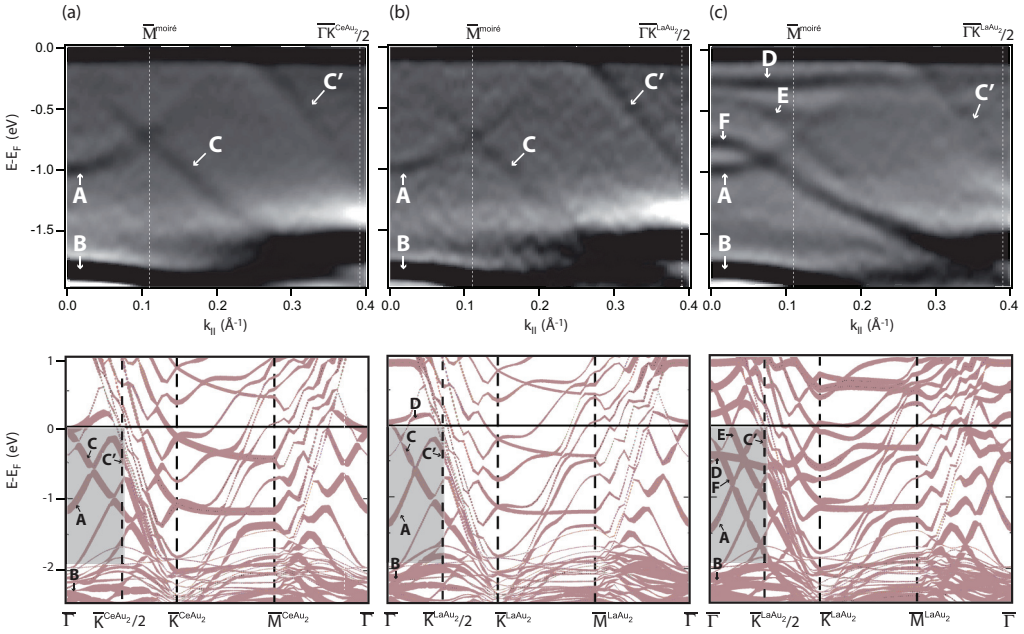

FIG. 5. (Color online) Top: Two-dimensional bands measured along the $\overline{\Gamma K}$ symmetry direction of (a) 1 ML CeAu$_2$, (b) 1 ML LaAu$_2$, and (c) 2 ML LaAu$_2$ surface intermetallic compounds. The different bands are labeled as in GdAu$_2$,[8] due to the clear analogy among the three different lanthanide intermetallic compounds. All the data correspond to the second derivative of the photoemission spectra, and have been measured with $h\nu = 44$ eV for CeAu$_2$, and $h\nu = 33$ eV for LaAu$_2$. The corresponding bands for GdAu$_2$ have been published elsewhere.[8] Bottom: corresponding theoretical band structures. The $\overline{\Gamma K M \Gamma}$ symmetry directions refer to those of the LaAu$_2$ 2D crystal. The width of the bands gives the relative weight of orbital projections on the $m = 0$ channel for all angular momenta. Relative shifts (in particular for 2 ML LaAu$_2$) are due to the imposition of commensurability with the substrate and the large resulting strain. The spin-up polarization is shown for the CeAu$_2$.

the second layer of CeAu$_2$ is not actually being formed in the ARPES experiments, probably due to an excess annealing temperature.

The top panels in Fig. 5 show the band structure measured along the $\overline{\Gamma K}$ symmetry direction[20] of the CeAu$_2$ ML [panel (a)], the LaAu$_2$ ML [panel (b)], and the LaAu$_2$ bilayer [panel (c)]. The data correspond to the second derivative of the photoemission intensity, which allows us to enhance band features over the intense steep background (see Fig. 7). For 1 ML, very similar A, B, C, and C′ bands are identified in both CeAu$_2$ and LaAu$_2$, which are also analogous to those found for GdAu$_2$.[7] Band energies are listed in Table I for the three different REAu$_2$ compounds. Close to E_F, the A band has an electron-like parabolic dispersion around $\overline{\Gamma}$, whereas C disperses downward from the center of the zone $\overline{\Gamma}$, which is reached close to E$_F$. There is a sharp transition between 1 ML and 2 ML in LaAu$_2$ [see Figs. 5(b) and 5(c)], which involves the appearance of new bands near the Fermi level. In fact, the C band disappears and two new bands dispersing downward appear, E and F, with energy maxima at E-$E_F = 0.44$ and 0.77 eV. There is an additional flat band D very close to the Fermi level, which exhibits a small dispersion. An analogous transformation from 1 to 2 ML is also observed in GdAu$_2$.[8] We note that bands A and C for 1 ML cross each other at 0.74 eV and $k = 0.11$ Å^{-1}. This point coincides with the $\overline{M}$ point of the small and 30° rotated moiré Brillouin zone (BZ). The interaction with the moiré superlattice will be analyzed in more detail through constant energy surfaces in Fig. 6. Moreover, bands A and E in the 2 ML LaAu$_2$ band structure also appear to cross each other at the same k point. p-polarized light in normal emission ARPES geometry preferentially probes states with a nodal plane parallel to the surface, and hence band crossings such as those of Fig. 5 are expected to feature hybridization gaps. However, the hybridization gap is seen in the 2 ML A-E crossing of Fig. 5(c), but it is not detected in the corresponding A-C crossing of Figs. 5(a) and 5(b) for 1 ML alloys.

To understand the physical nature of the ARPES bands, we perform first-principles calculations in CeAu$_2$ and LaAu$_2$ monolayer and bilayer. The calculated bands are shown in the lower panels of Fig. 5. Here, high symmetry directions refer to the REAu$_2$ atomic lattice, and shaded areas mark the region explored with ARPES on top panels. To make an appropriate correspondence between theory and experiment, the thickness of the bands in the bottom part of Fig. 5 reflects the relative weight of the orbital projection along the $m = 0$ component of each channel. This corresponds to the largest contribution to the probability density probed in ARPES with p-polarized light and under near-normal emission. We must note the limits of the calculation, which is performed for strained alloy lattices which are forced to be commensurate with the underlying Au substrate, and also omit many-body and moiré effects. In these conditions the Fermi level (due to charge transfers) and bands (due to strain) will shift relative to each other, and relative to the substrate Au bands. We use the topological resemblance of the calculated bands with the data to identify and deduce the character of the ARPES bands.

The band labeled B is of pure Au-d character, having a significant probability at the substrate side of the interface.

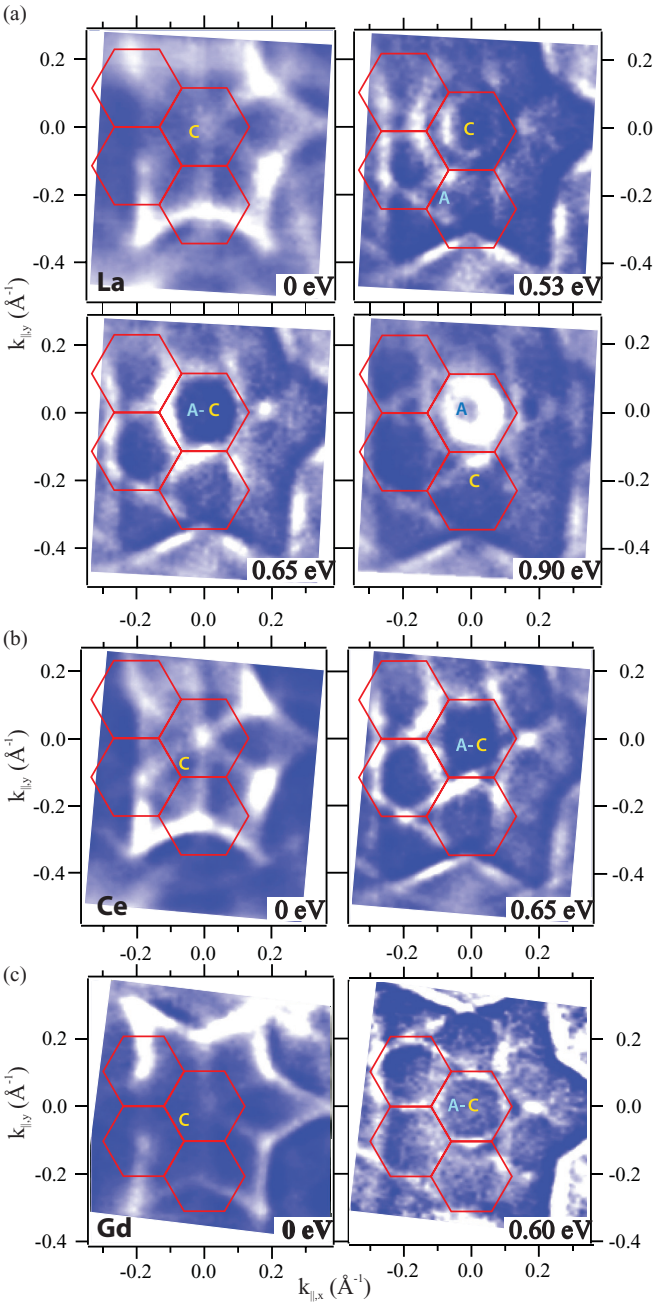

FIG. 6. (Color online) Constant energy surfaces at various energies for (a) 1 ML $LaAu_2$, (b) $CeAu_2$, and (c) $GdAu_2$, all measured with $h\nu = 44$ eV. Maps correspond to the second derivative of the photoemission intensity. Several hexagonal moiré Brillouin zones are indicated and the labels correspond to the ones used in Fig. 5. Some features appear replicated due to the moiré superlattice. At the Fermi level, the dominant intensity corresponds to the star-like band C′, which is brought to the zone center through moiré umklapps. At −0.65 eV in (a) and (b) and at −0.6 eV in (c), A and C merge into a single moiré-nested band.

Closer to E_F, the A band has La (Ce) d character with a contribution of Au-p electrons from the substrate and the intermetallic compound. The C band has a dominant Au-s nature, but it is also found to have a significant contribution from Au-d states of substrate Au atoms, which in turn dominate in C′. The C and C′ bands significantly couple to bulk Au states,

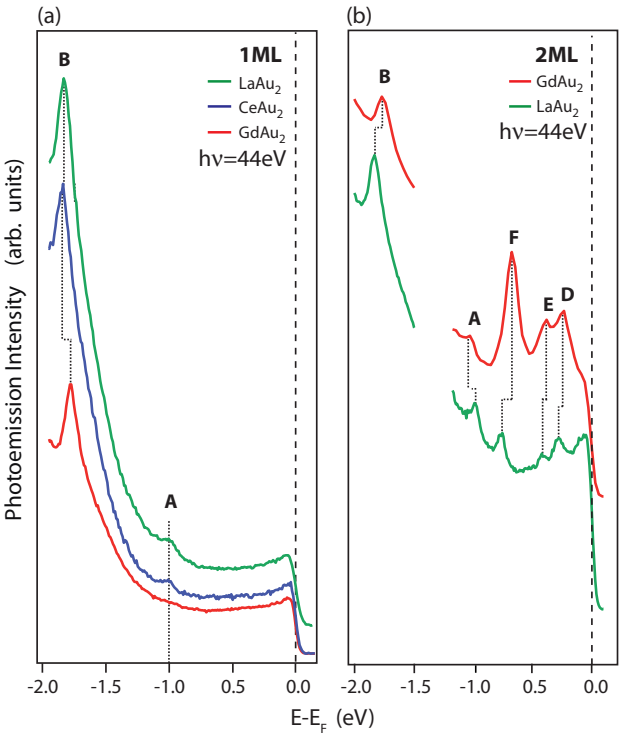

FIG. 7. (Color online) Energy distribution curves for (a) 1 ML and (b) 2 ML, as measured at $\overline{\Gamma}$ ($k_{||} = 0$) for the different $REAu_2$ surface alloys, including $GdAu_2$ from Ref. 7. Peak energies are listed in Table I.

explaining the slight dispersive behavior when changing the photon energy. None of these bands appear in the Au(111) bare substrate,[21] and hence all are spectroscopic signatures of the $LaAu_2$ ($CeAu_2$) surface intermetallic compound.

The analysis of the atomic orbital projections also gives some hints to understand the hybridization gap observed for A and E bands in the 2 ML, which is not visible in the corresponding 1 ML A-C crossing. In the 2 ML case the C band splits into E and F which have more weight localized in the substrate and in the ML, respectively. The F band character (Au-s in the ML) is orthogonal to A, whereas E has contributions from substrate orbitals, and interacts more strongly with A. One remarkable feature of the 2 ML $LaAu_2$ band structure in Fig. 5(c) is the strong, flat D band emission close to E_F. The D band corresponds to a mix of Au-p and La-d orbitals and is confined to the alloy. It appears unoccupied for 1 ML, and shifts below E_F in the 2 ML alloy.

In Fig. 6 we further investigate the topology of the 2D band structure of 1 ML alloys through constant energy surfaces. We represent again second-derivative image plots to enhance the visibility of the relatively weak features, particularly those arising from moiré lattice scattering. In Fig. 6(a) we show the maps for the $LaAu_2$ monolayer, whereas in Figs. 6(b) and 6(c) we select two characteristic surfaces for $CeAu_2$ and $GdAu_2$, measured at a photon energy of 44 eV. A, C, and C′ stand for the corresponding bands in Fig. 5. We have added the zone boundaries of the moiré network (hexagons) to the maps, whose periodicity can be otherwise determined from the replicas in almost all panels. Data in Fig. 6 in fact define moiré unit cells of (32 ± 2) Å for $LaAu_2$ and $CeAu_2$, and (35 ± 2) Å

TABLE I. Electronic band eergies at $\overline{\Gamma}$ ($k_{\|} = 0$) for 1 and 2 ML $REAu_2$ alloys, as measured with 44 eV photon energy and with respect to E_F. Labels refer to the distinct bands in Fig. 5. The C band energy is zero, since it crosses E_F at $\overline{\Gamma}$ in all cases. For the latter, we show the Fermi velocity measured at E_F with $h\nu = 44$ eV.

	Coverage	A (eV)	B (eV)	D (eV)	E (eV)	F (eV)	C [v_F(m/s)]
La	1ML	−1.02	−1.84				0.85×10^6
La	2ML	−1.02	−1.84	−0.30	−0.44	−0.77	
Ce	1ML	−1.00	−1.83				0.80×10^6
Gd	1ML		−1.78				0.74×10^6
Gd	2ML	−1.04	−1.77	−0.24	−0.39	−0.69	

for $GdAu_2$, values that agree well with the STM and LEED measurements and with previous results.[8]

At the Fermi level, the dominant star-like feature corresponds to the C′ band in all $LaAu_2$, $CeAu_2$, and $GdAu_2$. This is a Au-*d*-like state, which is nominally brought to the zone center through moiré umklapps, leading to mixing with the emerging C band of Au-*s* character. At 0.53 eV, C adopts a hexagonal shape that is tilted 30° with respect to the moiré Wigner-Seitz hexagon. This effect reflects the 30° rotation of the atomic lattice of the alloy with respect to that of the moiré. The most interesting moiré-driven hybridization scenario occurs at 0.65 eV in Figs. 6(a) and 6(b), and 0.6 eV in Fig. 6(c). At that point, A and C bands merge, leading to an A-C hybrid that is nested in the $\overline{M}$ point of the moiré BZ. Due to the 30° rotation of the hexagonally shaped bands, such nesting leads to a triangle-like hole-pocket at $\overline{K}$, which is particularly clear for $CeAu_2$ and $GdAu_2$.

The small spectral variations among the different lanthanide intermetallic compounds are better accounted for in energy distribution curves (EDCs) at a fixed $k_{||}$ value. EDCs at $\overline{\Gamma}$ for the whole series of 1 ML and 2 ML alloys are shown in Fig. 7. Energies for the different transitions are summarized in Table I. C is absent in these EDCs. The C band appears cut off by the Fermi level, and hence a comparative analysis of its Fermi velocity (measured at similar photon energies for the three alloys) is included in Table I. The lanthanide *d*-like A band has its minimum binding energy at 1.02 eV for $LaAu_2$, although it shifts only 20 meV from La to Ce or Gd and from 1 ML to 2 ML, i.e., a small variation that falls within the experimental accuracy. Also for C, Fermi velocity values around 0.8×10^6 m/s are found in all cases. We conclude that in 1 ML thick intermetallic compounds there are no major differences among the lanthanides [Fig. 7(a)]. In contrast in 2 ML alloys, A, B, D, E, and F bands exhibit a large variation of 50–80 meV from Gd to La. We note that A, which has a larger probability on lanthanide atoms, shifts in the opposite direction than B, D, E, and F, which have more weight in Au atoms. This strongly suggests that the shift in Fig. 7(b) is probably of chemical nature, i.e., it depends on the type of lanthanide that makes up the surface alloy.

IV. CONCLUSION

We have investigated the structure and electronic properties of two novel intermetallic compounds, $LaAu_2$ and $CeAu_2$, comparing them with the already studied $GdAu_2$ case.[7,8] By STM we observe a complete structural analogy with similar moiré and atomic lattice periodicity that vary slightly depending on the lanthanide atom. The electronic structure has been analyzed by ARPES through two-dimensional band dispersion, constant energy surfaces, and energy distribution curves spectra, also offering an overall resemblance over the different alloys. The physical-chemical nature of each electronic band has been clarified by direct comparison with first-principles calculations performed for monolayers and bilayers. Beyond the pure identification of the measured bands, the calculation has allowed us to understand the nature of electronic states that mix through scattering with the moiré superlattice.

ACKNOWLEDGMENTS

This work was supported in part by the Spanish MICINN (MAT2010-21156-C03-01 and -C03-03) and the Basque Government (IT-621-13). The SRC is supported by the NSF under Grant No. DMR-0537588. The authors acknowledge an A.R.C. grant (TheMoTherm 10/15-03) from the CfBelgique and financial support from the Gipuzkoako Foru Aldundia. Computer time was made available by PRACE-2IP DECI-8 (EU FP7 Grant No. RI-283493) and the Belgian CECI.

[1] M. Ruff, N. Takehiro, P. Liu, J. K. Nørskov, and R. J. Behm, Chem. Phys. Chem. **8**, 2068 (2007).

[2] J. Greeley, I. E. L. Stephens, A. S. Bondarenko, T. P. Johansson, H. A. Hansen, T. F. Jaramillo, J. Rossmeis, I. Chorkendorff, and J. K. Nørskov, Nat. Chem. **1**, 552 (2009).

[3] L. Fernández, M. Corso, F. Schiller, M. Ilyn, M. Holder, and J. E. Ortega, Appl. Phys. Lett. **96**, 013107 (2010).

[4] H. Brune, M. Giovannini, K. Bromann, and K. Kern, Nature **394**, 451 (1998).

[5] N. Nilius, E. D. L. Rienks, H. P. Rust, and H. J. Freund, Phys. Rev. Lett. **95**, 066101 (2005).

[6] A. T. N'Diaye, S. Bleikamp, P. J. Feibelman, and T. Michely, Phys. Rev. Lett. **97**, 215501 (2006).

[7] M. Corso, M. J. Verstraete, F. Schiller, M. Ormaza, L. Fernández, T. Greber, M. Torrent, A. Rubio, and J. E. Ortega, Phys. Rev. Lett. **105**, 016101 (2010).

[8] M. Corso, L. Fernández, F. Schiller, and J. E. Ortega, ACS Nano **4**, 1603 (2010).

[9]L. Fernández, M. Blanco-Rey, M. Illyn, L. Vitali, A. Correa, P. Ohresser, J. E. Ortega, A. Ayuela, and F. Schiller (unpublished).
[10]D. Givord, in *Magnetism and Synchrotron Radiation*, Lecture Notes in Physics, Vol. 565, edited by E. Beaurepaire, F. Scheurer, G. Krill, J.-P. Kappler (Springer, New York, 2001).
[11]I. D. Hughes, M. Dane, A. Ernst, W. Hergert, M. Luders, J. Poulter, J. B. Staunton, A. Svane, Z. Szotek, and W. M. Temmerman, Nature **446**, 650 (2007).
[12]Z. Fisk, D. W. Hess, C. J. Pethick, D. Pines, J. L. Smith, J. D. Thompson, and J. O. Willis, Science **239**, 33 (1988).
[13]J. Li, W. D. Schneider, R. Berndt, and B. Delley, Phys. Rev. Lett. **80**, 2893 (1998).
[14]F. Patthey, J.-M. Imer, W.-D. Schneider, H. Beck, Y. Baer, and B. Delley, Phys. Rev. B **42**, 8864 (1990).
[15]A. C. Hewson, *The Kondo Problem to Heavy Fermions* (Cambridge University, New York, 1993).
[16]X. Gonze, B. Amadon, P.-M. Anglade, J.-M. Beuken, F. Bottin, P. Boulanger, F. Bruneval, D. Caliste, R. Caracas, M. Côté *et al*., Comp. Phys. Comm. **180**, 2582 (2009).
[17]P. E. Blöchl, Phys. Rev. B **50**, 17953 (1994).
[18]V. I. Anisimov, J. Zaanen, and O. K. Andersen, Phys. Rev. B **44**, 943 (1991).
[19]S. Ma, X. Zhao, J. A. Rodriguez, and J. Hrbek, J. Phys. Chem. C **111**, 3685 (2007).
[20]The band structure in Fig. 5 actually corresponds to a k direction tilted 5° degrees from $\overline{\Gamma K}$. The correct band structure along $\overline{\Gamma K}$ has been obtained during the Fermi surface mapping, although restricted to a narrower energy range down to -1.0 eV. Within this range, it shows no appreciable difference from Fig. 5.
[21]C. B. Sommers and H. Amar, Phys. Rev. **188**, 1117 (1969).